Check for updates

Enhanced spin lifetime in colloidal quantum dots by growth from singly Mn-doped molecular cluster seeds†

Julian Schneider,[a] Chris Page,[a] James Harris,[a] Nigel L. Pickett,[a] Nathalie C. Gresty,[a] Christopher Waby,[a] Charles Biddlecombe,[a] Rachel M. Barrett,[b] Adam Brookfield,[c] Patrick Parkinson, [ID] [b] Floriana Tuna, [ID] [c] Simon M. Fairclough[d] and David J. Binks [ID] *[b]

Doped colloidal quantum dots (CQDs) are promising spin–photon interfaces, combining excellent optical properties and a substrate-free, nano-positionable platform. Here, we report the synthesis of InP/ZnSeS core–shell CQDs from zinc sulphide based seed clusters containing single Mn(II) ions. The resulting doped CQDs demonstrate photoluminescence quantum yields of up to 70%, a spin–lattice lifetime of 22 ms and a spin coherence lifetime of 2.7 μs, greater than and similar to the best yet reported for Mn-doped CQD systems, respectively. These spin lifetimes were achieved despite the high nuclear spin of InP, demonstrating the effectiveness of the ZnS cluster in shielding the Mn ion from its environment.

Introduction

Colloidal quantum dots (CQDs) are individual semiconductor nanocrystals that can be synthesized by solvent-based chemistry and are small enough in size to confine the wave-functions of carriers within them. The resultant size-tuneability of their properties, coupled with their excellent optical performance and the versatility of the synthetic techniques by which their composition and structure can be controlled, has led to their development for numerous applications including LEDs and displays,[1,2] photovoltaic cells,[3] photodetectors,[4,5] and biological imaging.[6,7]

The optical and electronic properties of CQDs can be modified by impurity doping. Initial attempts at CQD doping encountered unexpected difficulties with impurity atoms often being expelled due to a defect formation energy that increases with decreasing CQD size, an effect known as 'self-purification'.[8] However, these challenges were eventually overcome when a better understanding of the process of impurity adsorption was developed.[8] Doping CQDs with just one impurity atom each enables several applications. Early work was motivated by the magneto-optic properties of singly doped CQDs and their potential use in spintronics.[9,10] More recently, the potential of singly doped CQDs for application in quantum technologies such as quantum memory has been recognised.[9,11,12] The spin states of the dopant atom can be used to store an optically addressable qubit and there are several benefits that come from locating the dopant within a CQD. The dopant can be coupled to the CQD exciton *via* an exchange interaction[13] enabling it to be addressed by manipulating the exciton, as has been demonstrated for a singly Mn-doped self-assembled quantum dot.[14] The CQD, and thus the dopant coupled to its exciton, can have an optical cross-section of up to 100 Debye,[15] 3–5 orders of magnitude greater than an isolated dopant atom.[16] The nature of the CQDs as isolated, substrate-free nanocrystals enables their incorporation into photonic structures by pick-and-place techniques.[17,18] Finally, the use of the well-developed tool box of CQD synthetic techniques to determine the composition and structure enables the environment surrounding the dopant to be precisely controlled; an example of the benefit of this is the extension of spin lifetimes achieved by the growth of a shell around the QD core, thereby isolating the dopant from surface spins.[19]

However, the potential benefits of singly doped CQDs as a platform for quantum memory have yet to be realised because of the stochastic nature of the doping techniques used to date. The impurity is typically introduced during CQD synthesis at a

[a]*Nanoco Technologies Ltd, The Heath Business & Technical Park, Runcorn, Cheshire, WA7 4QX, UK*

[b]*Department of Physics and Astronomy & Photon Science Institute, University of Manchester, Manchester M13 9PL, UK.*
E-mail: david.binks@manchester.ac.uk

[c]*Department of Chemistry and Photon Science Institute, University of Manchester, Manchester, M13 9PL, UK*

[d]*Department of Material Science and Metallurgy, University of Cambridge, 27 Charles Babbage Road, Cambridge, CB3 0FS, UK*

†Electronic supplementary information (ESI) available. See DOI: https://doi.org/10.1039/d4nr04558k

concentration corresponding to approximately one atom per CQD on average but is randomly incorporated.[8] There is thus a distribution of the number of dopants per CQD about this average, meaning that the resulting population of CQDs must be searched and tested until an example of a singly doped CQD is identified. Moreover, the location of the dopant within the CQD volume also varies probabilistically between CQDs, resulting in a significant variation in the exchange interaction that couples the dopant to the CQD exciton, which depends on the wave-function overlap between them and hence the dopant location.[13]

A 'molecular seeding' approach has been used to precisely dope CQDs with several dopant ions, with the number being controlled by the composition of the seeding cluster.[20–23] This paper introduces a deterministic doping approach for the synthesis of singly doped CQDs. This is achieved *via* the stepwise synthesis of zinc sulphide molecular clusters, each doped with a single Mn atom. These clusters are then used as the seeds for the growth of CQDs, ultimately resulting in the deterministic single doping of CQDs. The resulting CQDs show good optical and electronic properties, exhibiting a photoluminescence quantum yield (PLQY) of up to 70%. The spin–lattice lifetime, T_1, and the spin coherence lifetime, T_2, which characterise the relaxation of the longitudinal and transverse components of the spin (relative to the applied magnetic field), respectively, can be extended to $T_1 = 22$ ms and $T_2 = 2.7$ µs by increasing the size of the seed cluster. The spectral diffusion lifetime, T_{SD}, which characterises the interaction of the spin with its surroundings, increases from 0.37 ms to 4.4 ms as the seed cluster size is increased, indicating a reducing influence of the environment.

Results

The synthetic route used to fabricate the singly Mn-doped core/shell InP CQDs is illustrated in the scheme shown in Fig. 1. To build the CQDs from the bottom up approach, the first step involves the synthesis of a Mn(II) complex with four coordinated sulphur linking sites.[24] This complex acts as the central unit for the growth of molecular zinc sulphide clusters *via* the reactive sulphur sites. Zinc sulphide growth is initiated by replacing $SiMe_3$ groups with $ZnCl_2$ tetramethylethylenediamine (tmeda), forming a Mn–S–Zn complex intermediate. This intermediate is further reacted step-wise with molecular building blocks of $Zn(SSiMe_3)_2(tmeda)$ and $ZnCl_2(tmeda)$ in alternating additions. Varying the number of cycles and precursor amounts further allows cluster size tunability, with sizes being limited by their colloidal solution stability in the presence of tmeda ligands. Two cluster sizes were synthesised for this study, termed 'small' and 'large' from hereon in, with further details of their growth given in the ESI.† By choosing appropriate reaction conditions, this approach aims to maximise individual cluster growth while minimising cross-bonding between multiple Mn(II) complexes, yielding a large number of molecular zinc sulphide clusters containing single Mn(II) dopants.

In the next step, Mn-doped zinc sulphide clusters are used as seeds in the colloidal synthesis of InP QDs. Following the same principles of avoiding cluster or QD aggregation at the early stages of growth required the use of reactive precursors ($P(SiMe_3)_3$) and mild reaction conditions (*e.g.* room temperature). After the initial nucleation, additional growth of InP was conducted at elevated temperatures (180–250 °C). Varying the number of clusters used relative to the amounts of the other reagents enabled control over the spectral position of the first absorption peak, which corresponds to the average CQD size (see the ESI†). Increasing the number of clusters resulted in the nucleation of more dots and thus a smaller average CQD size since the other reagents are now shared among a greater number of nucleation centres. This indicates that the CQDs are templating around the cluster ensuring single doping of the final CQDs. Finally, the CQDs were shelled with a compositionally graded shell of ZnSeS aiming to suppress surface traps and boost photoluminescence quantum yields.

Fig. 2a shows the absorbance and photoluminescence (PL) spectra for the Mn–S–Zn complex and the Mn-doped ZnS cluster. In both cases, the absorbance grows strongly with decreasing wavelength below about 300 nm, in agreement with spectra reported for these clusters previously.[25] While the Mn–S–Zn complex is featureless, the Mn-doped ZnS cluster shows a defined transition at 257 nm, emerging from an increasing number of S–Zn interactions. The PL spectrum, recorded at an excitation wavelength of 255 nm, is broad for each stage, extending from about 550 nm to 750 nm; however, the PL peak for the cluster centred at 600 nm is blue-shifted by about 20 nm compared to the peak for the complex. This is linked to the change in the local environment because of the ZnS cluster formation, such as a change in the Mn–S separation, for example. In both cases the emission is consistent with the $^6A_1$–$^4T_1$ transition in Mn(II). These results show that the absorption properties of these compounds are dominated by ZnS, while emission occurs *via* the embedded Mn(II) ions.

The optical properties of the CQDs are displayed in Fig. 2b, which shows a series of absorbance spectra that track the growth of InP on the Mn-doped ZnS molecular cluster. In the presence of the cluster, early formation of InP is indicated by a change in colour from colourless to yellow upon addition of indium carboxylate to the cluster and tris(trimethylsilyl)phosphine at room temperature. This is further reflected by the formation of an absorption peak at 360 nm. Further growth of InP occurs after heating the solution slowly to 200 °C, as shown by the formation of an absorption peak at 435 nm. After the initial growth of InP at lower temperatures, additional growth was conducted at 250 °C with the final core material having an absorption peak at 507 nm. The PL of the Mn-doped core-only QDs is dominated by the excitonic band edge PL; however, PLQYs are low due to the poor surface passivation of pure InP QDs. This was addressed by the growth of a ZnSeS alloyed shell, resulting in a final QD structure of ZnS:Mn/InP/ZnSeS.

Fig. 2b also shows the optical properties of the final shelled material after the growth of the ZnSeS shell. The growth of this
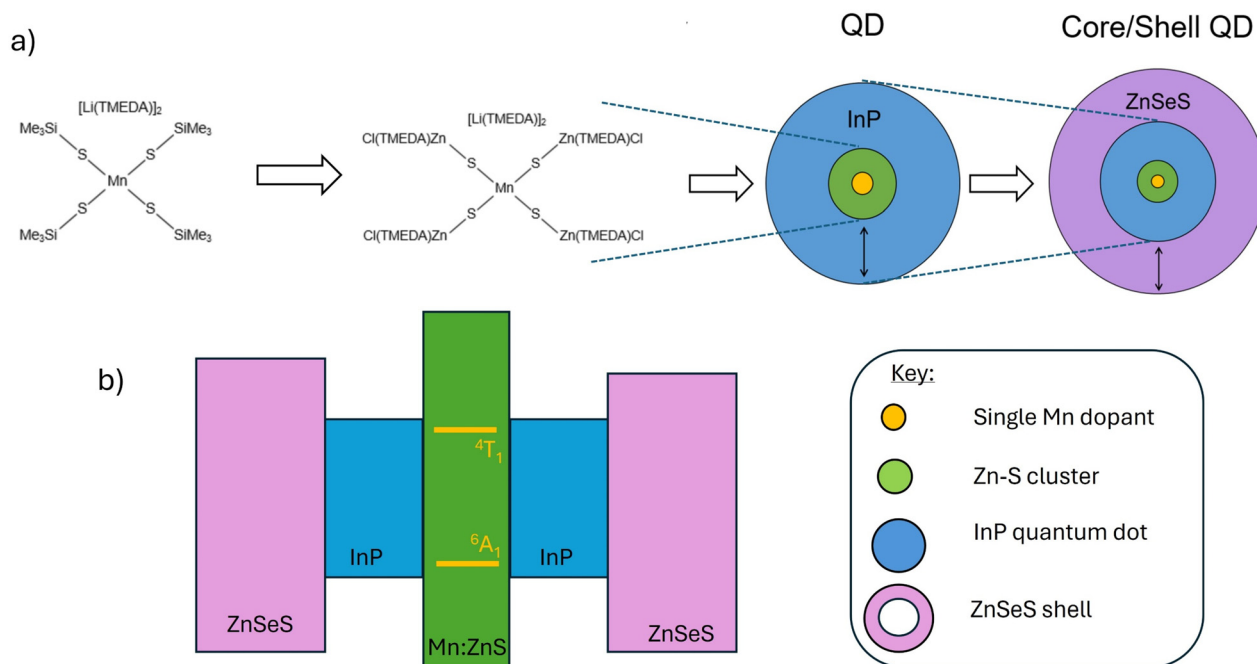
Fig. 1 (a) Schematic introducing the structure of a deterministically doped CQD and the multi-step bottom-up approach to achieve this. Synthesis starts from a four coordinated Mn(II) complex with four reactive anchoring sites. This coordination facilitates the step-by-step selective growth of molecular ZnS clusters, which can further be used as seeds for the growth of CQDs. These CQDs are shelled following standard type I shelling principles with the aim of improve emission properties. Cluster and CQD sizes can be tuned by varying the synthesis conditions and precursor amounts, thus providing a large platform to tune and tailor the resulting excitonic properties. An indicative energy diagram is shown in (b).

shell results in a red-shift of the absorption and emission peaks with an absorption peak centred at 544 nm corresponding to the lowest energy optically allowed valence band to conduction band transition ($1S_e$–$1S_{3/2}$) in the CQD.[26,27] The PL spectrum peak at 585 nm has a FWHM of 52 nm. The PL peak is asymmetrical with an extended long wavelength side. This emission tail coincides with the emission band from the cluster associated with the Mn $^6A_1$–$^4T_1$ transition,[28] although it is also possibly due to surface trap related emission. The PLQY for this sample was found to be 68%.

High angle annular dark field (HAADF) transmission electron microscopy (TEM) and energy dispersive X-ray spectroscopy (EDS) were used to examine the size and composition of the CQDs. Fig. 3a and b show the TEM images of the CQDs at lower and higher magnification, respectively. The distribution of CQD sizes obtained from the TEM measurements is given in the ESI† and has an average of 5.3 nm and a standard deviation of 16%. Dynamic light scattering measurements were also used to assess the size of the CQDs before and after the addition of the shell – see the ESI.† Fig. 3a shows that the InP/ZnSeS CQDs have a tetrahedral morphology, as expected since InP cores can form as regular tetrahedra.[29,30] Fig. 3b shows a TEM image with visible lattice fringes; the associated diffraction pattern (see Fig. 3c and d) corresponds to a zinc blende crystal structure with a lattice constant of 5.57 Å, which lies between the values for zinc blende ZnSe (5.67 Å) and ZnS (5.41 Å),[31] as expected for a ZnSeS shell. EDS images of the CQDs are given in the ESI (Fig. S1†). As expected for InP/ZnSeS

core/shell CQDs, the distribution of each element throughout the image is similar but with a weaker signal for In and P due to their presence in the core only. The imaging of single Mn dopant atoms within a CQD is challenging but has been demonstrated previously for Mn-doped ZnSe CQDs.[32] Using a similar approach, electron energy loss spectroscopy (EELS) was used to locate the presence of Mn-dopants within the CQDs. Fig. 3e shows an EELS image of several CQDs with Fig. 3f and g showing the EELS spectra in the range of the L_2 and L_3 Mn peaks at two example pixels in this image, with associated Gaussian fits; EELS spectra for further points are given in the ESI.† The positions of these two peaks agree with previous reports for MnS.[33] Fig. 3f corresponds to a CQD and shows that the amplitudes of the Mn L_2 and L_3 peaks are about 3 and 2 times the noise level, respectively; previous work on the detection of single Mn atoms in CQDs had found similar signal to noise levels.[32] For comparison, Fig. 3g shows the EELS spectrum for a background pixel. Attempted fits to the Mn L_2 and L_3 transitions are shown, but in this case, the resulting peaks are similar to the noise level, consistent with the absence of Mn at this pixel. Thus, the EELS data are consistent with the CQDs containing single Mn dopants, as expected.

To probe the spin dynamics of single Mn dopants encapsulated in the quantum dots, low frequency electron paramagnetic resonance (EPR) spectroscopy measurements were performed. Fig. 4a shows the EPR spectrum at 9.4 GHz of Mn-doped CQDs grown from the small cluster; the ESI† contains
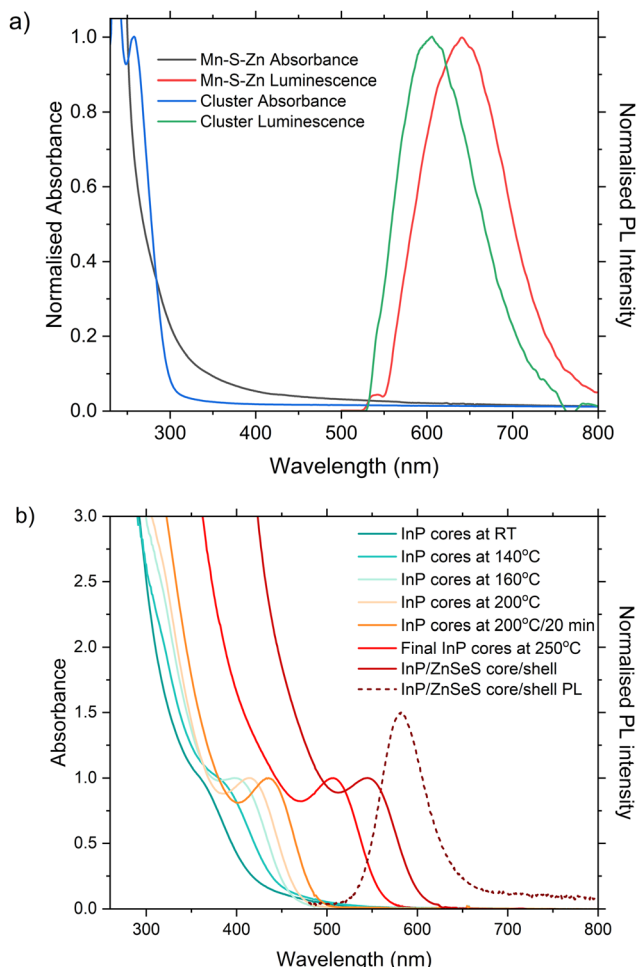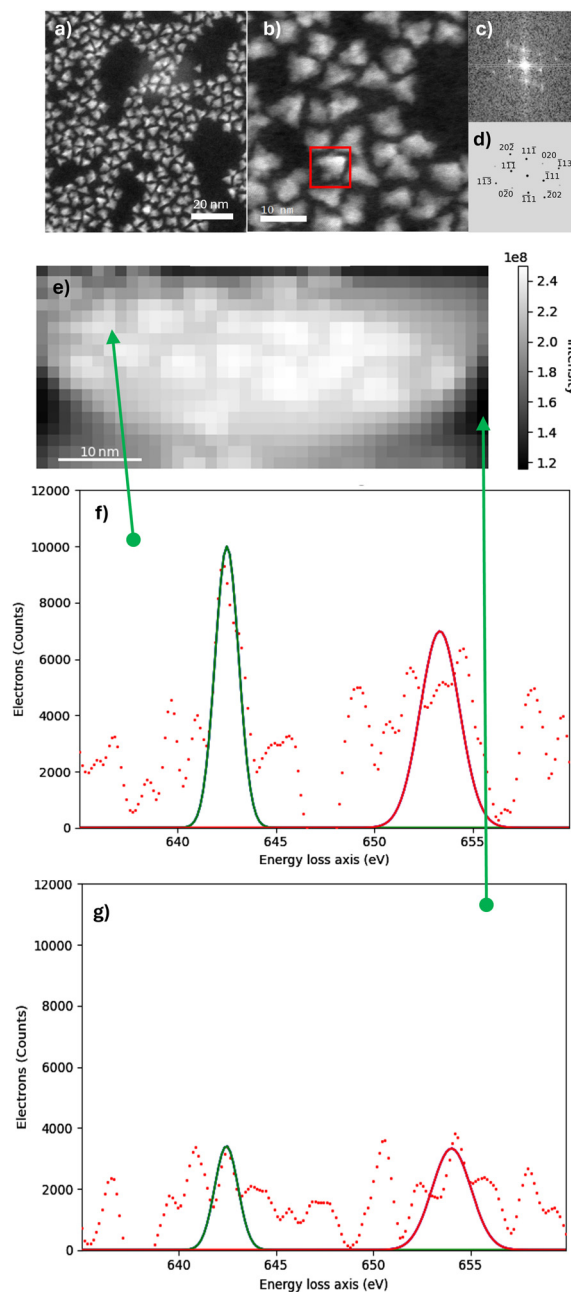
Fig. 2 (a) Absorbance and PL spectra of the Mn–S–Zn complex and the small ZnS:Mn seed cluster. (b) Absorbance spectra showing the growth of the InP core from the small seed cluster with increasing temperature and reaction time. Growth to the final core wavelength of 507 nm was done at 250 °C. Also shown are the absorbance and PL spectra for the core/shell InP/ZnSeS CQDs.
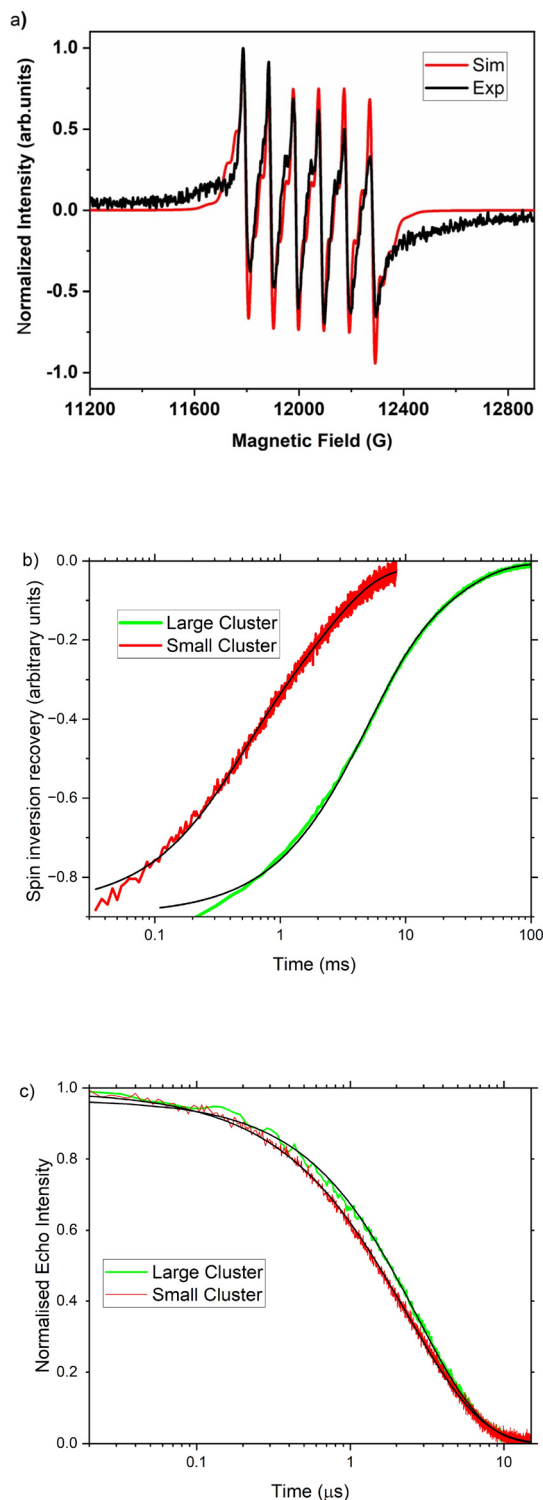

Fig. 3 HAADF TEM images with (a) an array of core/shell CQDs and (b) a close-up of few individual nanocrystals. (c) Diffraction pattern for the CQD identified by a red box in (b). (d) Miller indices for the diffraction spots seen in (c). (e) An EELS image of several CQDs with EELS spectra (red dashes) for two example points in the region of the Mn $L_{2,3}$ transitions, indicating the (f) presence or (g) absence of Mn atoms. Also shown in (f) and (g) are Gaussian fits to the Mn L_2 (green solid line) and L_3 (red solid line) peaks. The spectra for further points are shown in the ESI.†

similar data for the large cluster. Six well-resolved hyperfine transitions are visible, in full agreement with the $3d^5$ high-spin configuration of Mn^{2+} ($S = 5/2$, $I = 5/2$, $L = 0$), with the $^6A_1$ ground state.[34] This configuration is associated with five electronic transitions, of which only the $m_s = -\frac{1}{2}$ to $m_s = +\frac{1}{2}$ transition displays a 6-line pattern indicative of hyperfine coupling to $^{55}Mn^{2+}$ ($I = 5/2$; natural abundance 100%[35]). The other transitions are usually broadened by zero-field splitting (ZFS) effects.[36] The EPR spectra were simulated using Easy Spin6.0[37] and considering the spin Hamiltonian,

$$H = \beta BgS + SDS + SAI, \qquad (1)$$

where g is the electronic g-tensor with principal values g_x, g_y and g_z, D is the ZFS tensor, defined by the axial ZFS parameter D and the rhombic term, E, A is a tensor with principal components A_x, A_y and A_z, describing the interaction between the S = 5/2 electron spin with the I = 5/2 nuclear spin of ^{55}Mn, while

S and I are electronic and nuclear spin operators. Fitting yielded $g = 2.007$, $A = 272$ MHz and $D = 0.1$ GHz, which are in good agreement with reported values for Mn-doped CQDs.[36] This good agreement between the simulated and experimental

Table 1 Spin–lattice (T_1), spectral diffusion (T_{SD}), and spin coherence (T_2) lifetimes for Mn-doped CQDs at temperatures of 5 K or less and for Mn concentrations of 1% or less

CQD type	T_1 (ms)	T_{SD} (μs)	T_2 (μs)	Ref.
CdSe	2.03	n/a	4.70	18
ZnO	0.298	46.6	1.18	18
ZnSe	0.184	26	0.84	31
PbS	10	27	8	32
InP/ZnSeS	22	4400	2.7	This work

EPR data indicates that Mn dopants are predominately in a single environment. Previous studies[38] of stochastically Mn-doped CQDs have shown that for Mn concentrations corresponding to an average of multiple Mn ions per CQD, the interaction between the dopants broadens these peaks significantly. However, when the concentration is reduced so that the average number of dopants per CQD is 1 or less, the peaks become narrow and well-resolved. For instance, when the concentration of Mn^{2+} was dropped to 0.1% in Mn-doped PbS CQDs, corresponding to an average of less than one Mn atom per CQD, the peak width was observed to decrease to less than 100 G, and thus a 6-line spectral pattern could be observed.[38] The EPR peaks shown in Fig. 4a are of a similar width or narrower, consistent with their growth from a seed cluster containing a single Mn^{2+} ion. Fig. 4b compares the spin–lattice decays for the Mn-doped core–shell CQDs grown from small and large clusters as measured by pulsed EPR spectroscopy. For both seed cluster sizes, the spin inversion decay, $A_{inv}(t)$, can be characterised by a biexponential decay:[39]

$$A_{inv}(t) = A_{inv}(\infty) + A_1 \exp(-t/T_1) + A_{SD} \exp(-t/T_{SD}) \quad (2)$$

where T_{SD} is the spectral diffusion lifetime and A_1 and A_{SD} are amplitude parameters. For the small seed cluster, fitting to eqn (1) yielded $T_{SD} = 0.37 \pm 0.02$ ms and $T_1 = 2.3 \pm 0.3$ ms, while for the larger cluster, higher values of $T_{SD} = 4.4 \pm 0.4$ ms and $T_1 = 22 \pm 2$ ms were found. The spectral diffusion is attributed to the influence of nearby non-zero spin isotopes, such as In-113 and In-115 (both $I = 9/2$ and together corresponding to 100% natural abundance[35]). The value for the large cluster is more than twice as long as the longest value reported previously for Mn-doped CQDs, as shown in Table 1. The spin coherence decays are shown in Fig. 4c. The decay of the echo intensity, $I_{echo}(t)$, for both cluster sizes is well described by a stretched exponential:

$$I_{echo}(t) = I_{echo}(0)\exp(-(t/T_M)^s) \quad (3)$$

where T_M is the phase memory lifetime and s is the stretch parameter. Fitting eqn (1) to the decays yields $T_M = 2.3 \pm 0.1$ μs and $s = 0.89 \pm 0.01$ for the small cluster, while for the large cluster, the fit produced values of $T_M = 2.7 \pm 0.1$ μs and $s = 1.01 \pm 0.02$. Fitting to all 6 transitions yielded the same relaxation times within 50 ns. Previous studies[19,36,40] have used the time constant derived from a single exponential fit to the spin coherence decay to determine T_2. Using this procedure for the

Fig. 4 (a) Comparison of the experimental EPR spectrum at 3 K using Q-band radiation to a simulated spectrum for CQDs grown from the small cluster. (b) Comparison of spin inversion decay at 3 K for the CQDs grown with the large ($B = 0.35$ T) and small ($B = 1.2$ T) clusters. Fits to eqn (2) are shown in black. (c) Comparison of the echo intensity decay at 5 K for CQDs grown from the large ($B = 3200$ G) and small ($B = 12\,000$ G) clusters. Fits to eqn (3) are shown in black.

large seed cluster CQD resulted in a good fit and a time constant, and hence a T_2 value of 2.7 ± 0.1 μs. As shown in Table 1, the value of T_2 determined for the large cluster is competitive with the longest value previously reported[19,36,40] for Mn-doped CQDs.

Discussion

Spin–lattice and spin-coherence lifetimes in doped CQDs are both reduced by the interaction of the dopant spin with other nearby spins, both nuclear and electronic.[19] This interaction is due to dipole–dipole coupling, which has a $1/r^6$ dependence (after averaging over possible Boltzmann-weighted spin orientations). A study that added an undoped CdSe shell onto a stochastically Mn-doped CdSe core found that a shell thickness of just 1 nm was sufficient to make the interaction between the spin on the Mn and the spins on the CQD surface negligible,[19] indicating that it is the spins of immediate atomic neighbours that have the most significant effect on spin lifetimes.

Even for CQDs grown largely free of defects, and thus of the associated spins, and with a shell that reduces the interaction with surface spins, a dopant at the CQD centre could still be exposed to nuclear spins. The use of a Mn-doped zinc sulphide molecular cluster as the seed around which a CQD is grown ensures that the atoms neighbouring the Mn dopants are nearly free of nuclear spins since naturally occurring sulphur and zinc contain 99% and 96% spin-0 isotopes, respectively.[35] In contrast, the atoms immediately neighbouring the Mn in stochastically grown CQDs often include elements with a lower natural abundance of the spin-0 isotopes. For instance, commonly used elements for CQDs such as Pb, Cd, Te and Se contain 22%, 8%, 8%, and 13% non-spin-0 isotopes, respectively.[35] The record T_1 value and the T_2 value which is competitive with the longest value reported for Mn-doped CQDs were obtained even though In and P are both spin rich elements; both of the naturally occurring indium isotopes, In-113 and In-115, have a nuclear spin of 9/2, while naturally occurring phosphorus is 100% P-31, which has a nuclear spin of $\frac{1}{2}$.[35] The obtained large T_1 and T_2 values that increase for the larger cluster size indicate that the zinc–sulphur cluster that surrounds the Mn is sufficient to significantly insulate the dopant spin from the surrounding InP spin bath. The growth of CQDs from a Mn-doped zinc–sulphur cluster thus not only allows deterministic, rather than stochastic, doping but also significantly reduces interactions with the surrounding spins. The use of the Mn-doped zinc–sulphur cluster thus enables a greater freedom to choose the elemental composition of the CQD to optimise its other properties without compromising the spin lifetimes of the dopant. Further increases in T_1 and T_2 can be anticipated *via* the use of isotopically selected sources of zinc and sulphur during the synthesis of the seed cluster, thereby ensuring that the immediate atomic environment of the Mn^{2+} ion is free of nuclear spins.

Conclusions

In this work, for the first time, CQDs are grown from zinc sulphide seed clusters which are doped with single Mn(II) ions. Tuning the cluster size enables the synthesis of CQDs with a record Mn dopant spin–lattice lifetime and a spin-coherence lifetime that is competitive with the longest lifetime reported so far. These lifetimes are both increased for larger clusters, which increases the size of the nearly spin-free volume surrounding the Mn dopant, significantly reducing the interaction with the spins in the rest of the CQD. This approach thus allows the composition of the CQD to be chosen to optimise its optical properties without significant impact on the spin lifetimes.

Experimental

Full details of the synthetic methods for each stage of the cluster growth and for the core/shell CQDs are given in the ESI.† Absorbance and photoluminescence (PL) spectra were obtained by diluting small amounts of the relevant solution or dissolving small amounts of the relevant solid in dry dichloromethane (DCM). PL spectra were typically recorded at an excitation wavelength of 255 nm, scanning a range from 300 to 800 nm. For the photoluminescence spectra, solutions were diluted to optical densities of between 0.1 and 0.2 at 255 nm. The spectra for the Mn–S–Zn complex and the seed cluster were recorded using a Horiba Jobin Yvon Fluorolog-3 (model FL3-22iHR) spectrofluorometer with a monochromated Xe lamp. The colloidal quantum dots were subjected to photoluminescence measurements on a Hamamatsu Quantaurus. Dynamic light scattering measurements were performed using a Malvern Zetasizer ZSU5700. The EPR instrument used was the Bruker ElexSys E580X spectrometer operating in pulse mode. Pulsed EPR was used to measure the spin inversion and spin echo decays at 3 K, with X band (9.4 GHz) excitation under a magnetic field of 0.32–0.035 T or Q-band (35 GHz) excitation under a magnetic field of ~1.2 T. Measurements of the spin–lattice relaxation time (T_1) were carried out with a magnetization inversion recovery pulse sequence (π–t–π/2–τ–π–τ–echo) with π/2 and π pulse lengths of 16 and 32 ns, respectively, fixed τ and variable t. Measurements of the phase memory time, T_m, were carried out using a Hahn echo sequence (π/2–τ–π–τ–echo) that implies a gradual increase of the inter-pulse delay, τ. The EPR spectra were obtained by calculating the derivative of the pulsed EPR signal. Electron microscopy was carried out using a Thermo Fisher Scientific 'Spectra' STEM with 4 EDS 'SuperX' detectors. A beam voltage of 120 kV was used monochromated to 100 meV. The beam current was 40 pA for high resolution imaging and 150 pA for EDS acquisition, and the convergence angle was 24 mrad. For EELS, the beam current was 100 pA with a collection angle of 30 mrad and was acquired using a Gatan Continuum 1066 with a 1 second dwell time with sub-pixel rastering.

View Article Online

Author contributions

D. J. B., P. P., N. L. P., J. H. and N. C. G. were responsible for project conceptualisation and funding acquisition. D. J. B. was also responsible for project administration and supervision and wrote the first draft of the manuscript and edited it. P. P. also contributed to supervision. The investigations were carried out by J. S., C. P., C. B., C. W. (synthesis), R. B. (optical measurements), A. B. and F. T. (EPR measurements), and S. F. (TEM, EDS and EELS measurements). All authors reviewed the manuscript.

Data availability

The data underlying this study are openly available at the University of Manchester Repository at **https://doi.org/10.48420/27317175**.

Conflicts of interest

There are no conflicts to declare.

Acknowledgements

References

1 Y.-H. Won, O. Cho, T. Kim, D.-Y. Chung, T. Kim, H. Chung, H. Jang, J. Lee, D. Kim and E. Jang, *Nature*, 2019, **575**, 634–638.

2 J. Kim, J. Roh, M. Park and C. Lee, *Adv. Mater.*, 2024, **36**, 2470153.

3 H. Aqoma, S.-H. Lee, I. F. Imran, J.-H. Hwang, S.-H. Lee and S.-Y. Jang, *Nat. Energy*, 2024, **9**, 324–332.

4 Y. Wang, L. Peng, J. Schreier, Y. Bi, A. Black, A. Malla, S. Goossens and G. Konstantatos, *Nat. Photonics*, 2024, **18**, 236–242.

5 S. N. S. Yadav, C. Hanmandlu, D. K. Patel, R. K. Singh, C.-Y. Chen, Y.-Y. Wang, C.-W. Chu, C.-T. Liang, C.-T. Lin, Y.-J. Lu and T.-J. Yen, *Adv. Opt. Mater.*, 2023, **11**, 2300131.

6 C. Finetti, L. Plavisch and M. Chiari, *Talanta*, 2016, **147**, 397–401.

7 S. Pandey and D. Bodas, *Adv. Colloid Interface Sci.*, 2020, **278**, 102137.

8 S. C. Erwin, L. Zu, M. I. Haftel, A. L. Efros, T. A. Kennedy and D. J. Norris, *Nature*, 2005, **436**, 91–94.

9 R. Fainblat, C. J. Barrows and D. R. Gamelin, *Chem. Mater.*, 2017, **29**, 8023–8036.

10 R. Fainblat, C. J. Barrows, E. Hopmann, S. Siebeneicher, V. A. Vlaskin, D. R. Gamelin and G. Bacher, *Nano Lett.*, 2016, **16**, 6371–6377.

11 R. M. Barrett and D. J. Binks, *Mater. Quantum Technol.*, 2023, **3**, 043001.

12 J. Almutlaq, Y. Liu, W. J. Mir, R. P. Sabatini, D. Englund, O. M. Bakr and E. H. Sargent, *Nat. Nanotechnol.*, 2024, **19**, 1091–1100.

13 R. Beaulac, Y. Feng, J. W. May, E. Badaeva, D. R. Gamelin and X. Li, *Phys. Rev. B: Condens. Matter Mater. Phys.*, 2011, **84**, 195324.

14 M. Goryca, T. Kazimierczuk, M. Nawrocki, A. Golnik, J. A. Gaj, P. Kossacki, P. Wojnar and G. Karczewski, *Phys. Rev. Lett.*, 2009, **103**, 087401.

15 M. Shim and P. Guyot-Sionnest, *J. Chem. Phys.*, 1999, **111**, 6955–6964.

16 C. R. Kagan, L. C. Bassett, C. B. Murray and S. M. Thompson, *Chem. Rev.*, 2021, **121**, 3186–3233.

17 H. A. Abudayyeh and R. Rapaport, *Quantum Sci. Technol.*, 2017, **2**, 034004.

18 A. W. Schell, G. Kewes, T. Schröder, J. Wolters, T. Aichele and O. Benson, *Rev. Sci. Instrum.*, 2011, **82**, 073709.

19 A. M. Schimpf, S. T. Ochsenbein and D. R. Gamelin, *J. Phys. Chem. Lett.*, 2015, **6**, 457–463.

20 A. M. Jawaid, S. Chattopadhyay, D. J. Wink, L. E. Page and P. T. Snee, *ACS Nano*, 2013, **7**, 3190–3197.

21 A. M. Mushtaq, S. M. Daniels and N. L. Pickett, *U.S. Patent*, 7588828, 2007.

22 J. Yu, H. Zhang, W. Xu, G. Liu, Y. Tang and D. Zhao, *Chem. Commun.*, 2021, **57**, 6448–6451.

23 B. Santiago-González, A. Monguzzi, V. Pinchetti, A. Casu, M. Prato, R. Lorenzi, M. Campione, N. Chiodini, C. Santambrogio, F. Meinardi, L. Manna and S. Brovelli, *ACS Nano*, 2017, **11**, 6233–6242.

24 C. B. Khadka, D. G. Macdonald, Y. Lan, A. K. Powell, D. Fenske and J. F. Corrigan, *Inorg. Chem.*, 2010, **49**, 7289–7297.

25 C. B. Khadka, A. Eichhöfer, F. Weigend and J. F. Corrigan, *Inorg. Chem.*, 2012, **51**, 2747–2756.

26 J. Kim, C. Y. Wong and G. D. Scholes, *Acc. Chem. Res.*, 2009, **42**, 1037–1046.

27 A. Brodu, M. V. Ballottin, J. Buhot, E. J. van Harten, D. Dupont, A. La Porta, P. T. Prins, M. D. Tessier, M. A. M. Versteegh, V. Zwiller, S. Bals, Z. Hens, F. T. Rabouw, P. C. M. Christianen, C. de Mello Donega and D. Vanmaekelbergh, *ACS Photonics*, 2018, **5**, 3353–3362.

28 S. Chakraborty, P. Mondal, M. Makkar, L. Moretti, G. Cerullo and R. Viswanatha, *Chem. Mater.*, 2023, **35**, 2146–2154.

29 G. Almeida, L. van der Poll, W. H. Evers, E. Szoboszlai, S. J. W. Vonk, F. T. Rabouw and A. J. Houtepen, *Nano Lett.*, 2023, **23**, 8697–8703.

30 K. Kim, D. Yoo, H. Choi, S. Tamang, J.-H. Ko, S. Kim, Y.-H. Kim and S. Jeong, *Angew. Chem., Int. Ed.*, 2016, **55**, 3714–3718.

31 L. I. Berger, *Properties of Semiconductors*, CRC Press, Boca Raton, 90th edn, 2009, pp. 12.80–12.81.

32 A. A. Gunawan, K. A. Mkhoyan, A. W. Wills, M. G. Thomas and D. J. Norris, *Nano Lett.*, 2011, **11**, 5553–5557.

33 C.-J. Chang, M.-C. Teng, J. Chen, Y.-G. Lin and C.-Y. Chen, *Appl. Surf. Sci.*, 2021, **558**, 149875.

34 A. Abragam and B. Bleaney, *Paramagnetic Resonance of Transition Ions*, Dover Publications, New York, 1986.

35 F. G. Kondev and S. Naimi, *Chin. Phys. C*, 2017, **41**, 030001.

36 J. K. Bindra, K. Singh, J. van Tol, N. S. Dalal and G. F. Strouse, *J. Phys. Chem. C*, 2020, **124**, 19348–19354.

37 S. Stoll and A. Schweiger, *J. Magn. Reson.*, 2006, **178**, 42–55.

38 F. Moro, L. Turyanska, J. Granwehr and A. Patanè, *Phys. Rev. B:Condens. Matter Mater. Phys.*, 2014, **90**, 205428.

39 A. Schweiger and G. Jeschke, *Principles of Pulse Electron Paramagnetic Resonance*, Oxford University Press, 2001.

40 F. Moro, L. Turyanska, J. Wilman, A. J. Fielding, M. W. Fay, J. Granwehr and A. Patanè, *Sci. Rep.*, 2015, **5**, 10855.